RESEARCH ARTICLE | JUNE 17 2024

Two-dimensional direct numerical simulation study of multicomponent mixing with phase transition in a transcritical shear layer

Alexander Doehring ✉ iD ; Theresa Trummler iD ; Michael Pfitzner iD ; Markus Klein iD

Check for updates

View Online

Export Citation

27 June 2024 13:51:33

Physics of Fluids

Special Topic:

John Michael Dealy (1937-2024): Celebrating His Life
Guest Editors: Alan Jeffrey Giacomin and Savvas G. Hatzikiriakos

Submit Today!

AIP Publishing

AIP Publishing
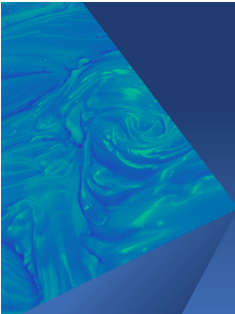
Two-dimensional direct numerical simulation study of multicomponent mixing with phase transition in a transcritical shear layer

View Online　　Export Citation　　CrossMark

Alexander Doehring,[1,a)] (iD) Theresa Trummler,[1] (iD) Michael Pfitzner,[2] (iD) and Markus Klein[1] (iD)

AFFILIATIONS

[1]Institute of Applied Mathematics and Scientific Computing, University of the Bundeswehr Munich, Werner-Heisenberg-Weg 39, 85577 Neubiberg, Germany
[2]Institute for Thermodynamics, University of the Bundeswehr Munich, Werner-Heisenberg-Weg 39, 85577 Neubiberg, Germany

[a)]Author to whom correspondence should be addressed: alexander.doehring@unibw.de

ABSTRACT

In this paper, we investigate two-dimensional direct numerical simulations of a transcritical shear layer. Three configurations are chosen, which are distinguished by the level of presence of two-phase phenomena. The thermodynamic model is based on a cubic equation of state. It was extended for multicomponent mixtures, and it is able to account for vapor–liquid equilibrium. The thermodynamic modeling with phase-transition is validated using experimental data from the literature. Special focus is put on the effect of the density gradient and the density changes caused by phase-transition on the development of the turbulent shear layer and the associated mixing. In addition to this, the vorticity distribution and the components of its transport equation are analyzed and compared for the different configurations.

I. INTRODUCTION

Today's requirement is to reduce greenhouse gas emissions demands for a higher engine efficiency. One possibility to enhance the efficiency of propulsion systems is to increases the operating pressure. Consequently, the critical pressure is exceeded, which raises the importance of intermolecular attractive and repulsive forces within the thermodynamic modeling of the fluid. Fluid features, such as gas-like diffusivity, liquid-like density, and vanishing surface tension are the consequences of the high pressure environment.[1]

The thermodynamic state of the fuel, oxidizer, and their mixture is determined by the pressure, temperature, and mixture fraction. As a result, a super-, trans-, and subcritical state is obtained in propulsion devices. The present study investigates the influence of different thermodynamic states on the shear layer dynamics employing direct numerical simulations (DNS).

In the past three decades, various experimental studies have been performed in order to understand the behavior of jets under supercritical or transcritical conditions. Mayer and Tamura[2] performed substantial experiments injection liquid oxygen (LOX) and gaseous hydrogen (GH$_2$) using a coaxial injector. At subcritical conditions, they showed the existence of droplets around the LOX jet and a diffuse mixing with the absence of droplets under supercritical conditions. Oschwald et al.[3] investigated the injection of liquid nitrogen into gaseous nitrogen. They confirmed the observations by Mayer and Tamura[2] and measured the axial and radial jet profiles. A review of the experimental efforts of sub-, trans-, and supercritical injection experiments has been made by Chehroudi.[4] He has measured the dark core length and proposed a model for the jet width growth rate in trans- and supercritical jets. Baab et al.[5] used laser-induced thermal acoustics to generate an experimental database for high-pressure jet mixing. They measured the speed of sound quantitatively, which can be used to validate numerical simulations.

In addition to experimental investigation, numerical simulations contribute to the understanding of transcritical mixing through the analysis of detailed three-dimensional (3D) distributions. Okong'o and Bellan[6] investigated a heptane nitrogen shear layer using direct numerical simulations in fully conservative formulation (FC). Analyzing the vorticity transport equations, they showed a dominant vorticity stretching and tilting responsible for the production of streamwise vorticity. Moreover, several studies showed that employing a fully conservative formulation may lead to unphysical pressure oscillations.[7–9] In this context, Ma et al.[10] developed a double flux method by

introducing an effective specific heat ratio based on the speed of sound. This method is able to prevent spurious pressure oscillations in transcritical flows but is non-conservative. Lacaze et al.[11] compared a fully conservative formulation applying an equation for the internal energy with two quasi-conservative (QC) methods, where the first method is based on a pressure equation and the second method couples a pressure and enthalpy equation. The latter formulation including the enthalpy equation is not fully conservative, but due to the coupling with the pressure equation, they achieved a suppression of spurious pressure oscillations and improved the temperature prediction, which is a drawback of a pure pressure equation formulation.[12,13]

Tudisco and Menon[14] simulated a spatial shear layer of hexane and nitrogen. In their study, either phase-separation effects have been calculated in terms of vapor–liquid equilibrium (VLE) or neglected (non-VLE). The shear layer with VLE was more fragmented, which leads to a faster breakup of the shear layer vortices. The importance of employing a phase-split calculation was also shown by Matheis and Hickel[12] performing an implicit large-eddy simulation (LES) of a non-reacting Spray-A from the Engine Combustion Network (ECN). Fathi et al.[15] extended the implicit LES for both reacting and non-reacting Spray-A. Additionally, they used an improved flash calculation replacing the isoenergetic-isochoric phase-splitting calculations (UV-flash) with isochoric-isothermal phase-splitting calculations (VT-flash)[16] for their comparison. Sharan and Bellan[17] analyzed the influence of thermodynamics and inflow conditions on round jets at sub- and supercritical conditions via DNS. They observed self-similarity of the mean axial velocity and the Reynolds stresses for high pressure flows. In addition, they concluded that the inflow conditions have a big impact, since the self-similar profiles are dependent on the inflow boundary conditions. Traxinger et al.[18] have used a similar thermodynamic modeling as Matheis and Hickel[12] but in the framework of a pressure-based LES in OpenFOAM. They compared their results with the spray images of Baab et al.[5] for three different cases, showing a good agreement in the spray formation and the presence of VLE regions. Begemann et al.[19] have used LES to validate the thermodynamic modeling including phase-splitting calculations. For this purpose, they employed several subgrid-scale (SGS) models and adjusted the interaction parameter for binary mixtures using experimental data.[5] A group at the City University London applied the Perturbed Chain Statistical Associating Fluid Theory (PC-SAFT)[20–22] equation of state (EoS) for their study of transcritical and supercritical jets.[23–25] They assessed in their studies the capabilities of PC-SAFT and showed a good agreement with experimental results for the ECN Spray-A.[26]

Although the significance of phase-split calculations has been strongly emphasized,[12,14,15] studies are conducted without VLE.[7,27–29] Furthermore, various studies did account for VLE but focused on the comparison between a fully conservative or a quasi-conservative formulation.[12,13,27,30]

In the present work, we investigate the influence of the non-linear thermodynamics with and without VLE on the shear layer dynamics. This is of great importance, since the mixing takes place within the shear layer, which further has an influence on the combustion and consequently on the performance of the propulsion system. We use DNS for this study in order to resolve all relevant scales and reduce the amount of modeling. For this analysis, we employ a 2D shear layer using propane and nitrogen. Three different cases with varying temperature and pressure conditions are used. In the first case

(2P), the adiabatic mixing temperature enters the two-phase region; hence, VLE is found in the shear layer. In the second case (C2P), the mixture slightly cuts the phase boundaries, and in the last case (N2P), the mixture is purely supercritical. We use the same thermodynamic modeling as presented by Matheis and Hickel[12] and Traxinger et al.[18] in order to account for real gas thermodynamics including VLE. To the authors' knowledge, this is the first DNS study of a shear layer for high pressure applications with two-phase mixing.

The current analysis differs from the following high pressure 2D shear layer studies. In the investigation of Tudisco and Menon,[14] the focus was on the comparison between VLE and non-VLE for a shear layer with a moderate resolution. Ma et al.[13] used a hydrogen and liquid oxygen shear layer to compare FC with QC. They did not state if the resolution fulfills DNS criteria. Unnikrishnan et al.[31] performed a DNS of a methane and liquid oxygen shear layer, but the chosen operating conditions did not allow VLE.

The presented study is based on 2D DNS of planar shear layers, which are not able to fully represent the dynamics of turbulence. However, it provides useful insight of how various thermodynamic states affect a transcritical shear flow. In addition, the obtained results are consistent with the physical expectations and the scaling of the individual terms of the vorticity transport equation.

The paper is structured as follows: The general configuration is introduced in Sec. II. The physical and numerical modeling are presented in Sec. III. Section IV presents the chosen operating conditions and the setup for the DNS simulations. The grid resolution and a grid study are provided in Sec. V. Results are analyzed in Sec. VI comparing all three cases. Finally, the paper is concluded in Sec. VII.

II. CONFIGURATION

In propulsion systems, various injectors are used in order to blend the fuel with the oxidizer. In Fig. 1, two examples are selected to demonstrate the mixing in an abstract way. A coaxial injector is shown at the top, which is found in rocket engines, and a single-hole injector is presented at the bottom, which is related to gasoline engines. Both applications are based on a supercritical pressure ($p > p_c$), whereas the temperature is below ($T < T_c$) or above ($T > T_c$) the critical temperature, respectively. Depending on the type of injector, several mixing or shear layers arise, as seen in Fig. 1. At subcritical conditions, primary and secondary atomization takes place within the mixing layer, leading to droplet formation. Purely supercritical mixing layers cannot produce any droplets, since the surface tension approaches zero, leading to a diffuse interface or diffuse mixing.[32,33] Both phenomena are found in transcritical mixing layers. Droplets and diffuse mixing can be observed since the critical point is a property of the mixture fraction resulting in a critical locus, which is both surpassed and undercut within the mixing layer.[34] Whether a subcritical state is obtained in a transcritical mixing layer depends on the operating pressure and temperature of the fuel and oxidizer. In this work, we aim to investigate a transcritical mixing layer (inner mixing layer) in the context of a coaxial injector.

III. PHYSICAL AND NUMERICAL MODELING

For the analysis of a transcritical mixing layer, we performed direct numerical simulations applying the compressible conservation equations for mass [Eq. (1)], momentum [Eq. (2)], and enthalpy [Eq. (3)]. Additional transport equations for species are included in Eq. (4).
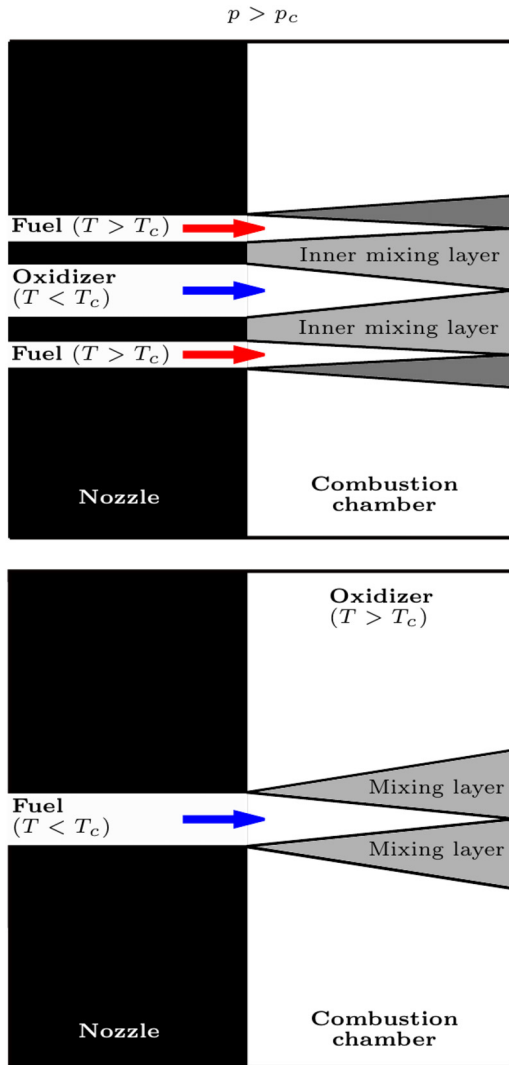
FIG. 1. Sketch of a coaxial injection (top) and a single-hole injector (bottom). The nozzle is on the left and the combustion chamber is on the right hand side. The pressure is above the critical pressure ($p > p_c$) for both injector types. The arrows indicate the direction of the injected fluid. The colors refer to the temperature of the injected fluid with blue for a temperature below the critical temperature ($T < T_c$) and red for a temperature above the critical temperature ($T > T_c$).

$$\frac{\partial \rho}{\partial t} + \frac{\partial (\rho u_i)}{\partial x_i} = 0, \tag{1}$$

$$\frac{\partial (\rho u_i)}{\partial t} + \frac{\partial (\rho u_i u_j)}{\partial x_j} = -\frac{\partial p}{\partial x_i} + \frac{\partial \tau_{ij}}{\partial x_j}, \tag{2}$$

$$\frac{\partial (\rho h)}{\partial t} - \frac{\partial p}{\partial t} + \frac{\partial \rho u_i h}{\partial x_i} = u_i \frac{\partial p}{\partial x_i} - \frac{\partial q_i}{\partial x_i} + \tau_{ij} \frac{\partial u_i}{\partial x_j}, \tag{3}$$

$$\frac{\partial (\rho Y_k)}{\partial t} + \frac{\partial (\rho u_i Y_k)}{\partial x_i} = -\frac{\partial j_{k,i}}{\partial x_i}, \tag{4}$$

where ρ, u_i, p, h, and Y are the density, velocity components, pressure, specific enthalpy, and mass fraction of the species, respectively. q_i

indicates the heat flux, and $j_{k,i}$ is the mass flux in direction x_i. The mass fraction Y_k is obtained by relating the mass of species k to the total mass, which is the sum of all masses

$$Y_k = \frac{m_k}{m_{tot}} \quad \text{with} \quad k = 1, \dots, N_k \tag{5}$$

$$\text{and} \quad m_{tot} = \sum_{i=1}^{N_k} m_i. \tag{6}$$

N_k is the number of used species. Per definition, the mass fractions of all components sum up to unity. Therefore, only one equation is solved for the mass fraction, since in this study we are dealing with binary mixtures ($N_k = 2$) and the seconds component is obtained as follows:

$$Y_2 = 1 - Y_1. \tag{7}$$

The viscous stress tensor τ_{ij} is calculated using Stokes' hypothesis. The mass and heat transfer is modeled by Fick's and Fourier's laws, respectively,

$$j_{k,i} = -\rho D \frac{\partial Y_k}{\partial x_i}, \tag{8}$$

$$q_i = -\lambda \frac{\partial T}{\partial x_i} + \sum_{k}^{N_k} h_k j_{k,i}. \tag{9}$$

Here, λ is the thermal conductivity, T is the temperature, and h_k is the partial enthalpy of species k. The diffusion coefficient D is assumed to be species independent and deduced from the heat diffusivity applying a constant Lewis number of $Le = 1$ (cf. Schmitt et al.[35]). Applying a Lewis number of one to Fourier's law [Eq. (9)] and including Fick's law leads to an enthalpy based formulation as follows:

$$q_i = -\frac{\lambda}{c_p} \left(\frac{\partial h}{\partial x_i} - \frac{\partial h}{\partial p}\bigg|_{T,Y} \frac{\partial p}{\partial x_i} \right), \tag{10}$$

where c_p is the specific heat capacity at constant pressure. The contribution of pressure changes to the heat flux is negligible in low Mach number flows. Thus, the enthalpy based formulation can be approximated as

$$q_i \approx -\frac{\lambda}{c_p} \frac{\partial h}{\partial x_i}. \tag{11}$$

In our study, we do not include Soret and Dufour effects, as well as gravity and heat radiation terms. The DNS simulations were conducted with a pressure-based version of OpenFOAM (see Refs. 18 and 36). The equations are discretized in space with a second order linear Gaussian scheme. For the time discretization, we employ a second order implicit backward scheme, which is provided by OpenFOAM by default. For the simulations, we have chosen a CFL number of 0.4 for accuracy reasons, which results in time steps of the order of 10^{-9} s.

A. Single component thermodynamic modeling

An additional equation is needed to relate the pressure to the density and temperature. We apply the Peng–Robinson (PR)[37] cubic equation of state (EOS). This EOS is able to reproduce the non-linear fluid behavior arising due to the high pressure environment in the investigated application. The general form of a cubic EOS is written as

TABLE I. Parameters for the Peng–Robinson EOS[37] used in the generalized cubic EOS in Eq. (12).

Parameter	Peng–Robinson
a	$0.457\,24\left(\dfrac{\mathcal{R}^2 T_c^2}{p_c}\right)$
b	$0.0778\left(\dfrac{\mathcal{R} T_c}{p_c}\right)$
u	2
w	-1
c	$0.374\,64 + 1.542\,26\omega - 0.2699\omega^2$
$\alpha(T)$	$[1 + c(1 - \sqrt{T_r})]^2$

$$p(\underline{v}, T) = \frac{\mathcal{R}T}{\underline{v} - b} - \frac{a\alpha(T)}{\underline{v}^2 + ub\underline{v} + wb^2}, \quad (12)$$

where pressure p is a function of the molar volume $\underline{v}$ and the temperature T. $\mathcal{R}$ is the universal gas constant of $8.314\,46\,\mathrm{J\,K^{-1}\,mol^{-1}}$, a accounts for intermolecular forces, and b is the repulsion parameter or the effective molecular volume. $\alpha(T)$ represents the fluid's polarity and is a correlation based on the acentric factor ω and the reduced temperature $T_r = T/T_c$. The subscript c refers to the critical point. u and w denote EOS constants. All parameters for the PR cubic EOS are summarized in Table I. For more details, see Poling *et al.*[1]

The transport properties viscosity η and thermal conductivity λ are modeled with correlations given by Chung *et al.*[38] The caloric properties c_v and c_p are computed with the departure function formalism.[1] Therefore, the reference quantity $c_{p,0}$ is obtained using NASA polynomials:

$$c_{p,0} = \mathcal{R}\left(a_1 + a_2 T + a_3 T^2 + a_4 T^3 + a_5 T^4\right). \quad (13)$$

The coefficients a_i are taken from Burcat *et al.*[39] The specific heat capacity at constant volume c_v is calculated using the universal gas constant and the reference specific heat at constant pressure $c_{v,0} = c_{p,0} - \mathcal{R}$. Using the reference value $c_{v,0}$, c_v can be calculated with

$$c_v = -TK \frac{\partial^2 a\alpha}{\partial T^2} - c_{v,0}. \quad (14)$$

K is a function of the cubic EOS parameters u, b, and w and reads

$$K = \frac{1}{b\sqrt{u^2 - 4w}} \ln\left[\frac{2v + b(u - \sqrt{u^2 - 4w})}{2v + b(u + \sqrt{u^2 - 4w})}\right]. \quad (15)$$

Based on the obtained c_v, we can calculate

$$c_p = c_v - T\left(\left.\frac{\partial p}{\partial T}\right|_{\underline{v}}\right)^2 \Big/ \left.\frac{\partial p}{\partial \underline{v}}\right|_T. \quad (16)$$

In the following, we analyze the applicability of the PR EOS for the considered configurations. Two of the three simulations, which have been performed, feature a chamber pressure of $p = 50$ bar and the temperature ranges from 200 to 600 K, as presented in detail in

Sec. IV. This results in a reduced pressure of $p_r = p/p_c = 1.18$ for propane. Figure 2 shows the density ρ and specific heat capacity c_p using PR EOS for propane. The Helmholtz energy equation of state (GERG-20004, GERG-2008) within the CoolProp library[40] serves as a reference. The thermodynamic modeling is able to reproduce the non-linear behavior for both quantities and is in good agreement with the reference data. A deviation from the reference data can be observed for the density at lower temperatures, as well as for the peak value of c_p. The profiles for nitrogen are not shown, since the pressure of $p = 50$ bar corresponds to a reduced pressure of $p_r = p/p_c = 1.47$ and the considered temperature range between 200 and 600 K result in an ideal gas behavior.

B. Multicomponent and multiphase mixtures

In propulsion systems, at least two fluids, a fuel and an oxidizer, are mixed together. In order to obtain fluid properties for a mixture, we apply a homogeneous-mixture single-fluid model. The concept is visualized in Fig. 3 inside one computational cell in the framework of a finite volume discretization. A cell-averaged solution is considered assuming a negligible slip between the two phases vapor and liquid. Thus, a reconstruction of the actual interface using a sharp-interface is not performed, and the surface tension is neglected.

The cubic EOS is adjusted for mixtures of N_k components by using general mixing rules for the following parameters:
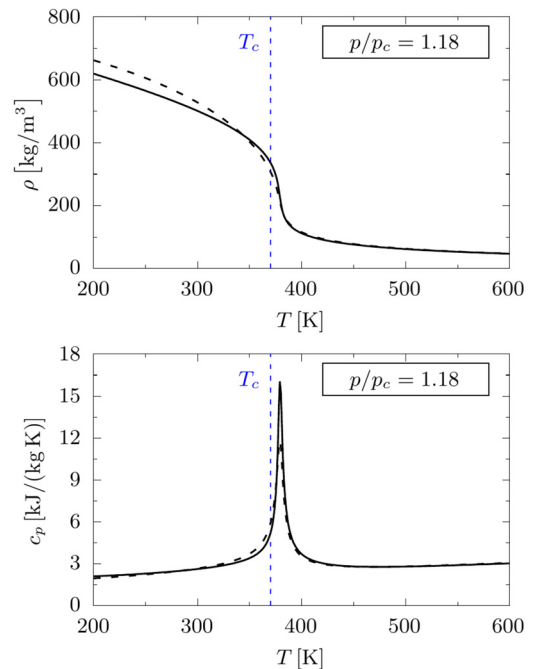
FIG. 2. Thermodynamic quantities: density ρ (top) and specific heat capacity c_p (bottom) of propane are presented as a function of the temperature. PR (dashed line) is compared with the Helmholtz energy equation of state (GERG-2004 and GERG-2008) taken from the CoolProp library[40] (solid line). The figures are generated using the python package realtpl.[41] The pressure is set to $p = 50$ bar, which results in a reduced pressure of $p_r = p/p_c = 1.18$. The critical temperature of propane of $T_c = 369.9$ K is included (blue dashed line).
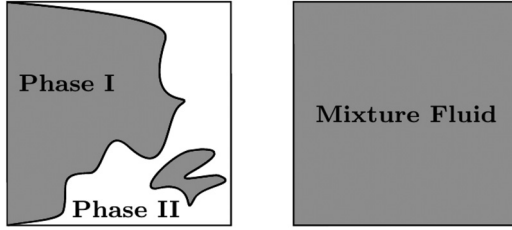
FIG. 3. Homogeneous mixture model inside one computational cell. Resolved phase interface (left) and homogeneous mixture (right).

$$a\alpha = \sum_{i}^{N_k} \sum_{j}^{N_k} z_i z_j a_{ij} \alpha_{ij},$$
$$b = \sum_{i}^{N_k} z_i b_i, \tag{17}$$

with the mole fraction z_i of component i. The coefficients a_{ij}, α_{ij}, and b_i are calculated according to Harstad *et al.*[42]

$$a_{ij}\alpha_{ij} = 0.45724 \frac{\mathcal{R}^2 T_{c,ij}^2}{p_{c,ij}^2} \left[1 + c \left(1 - \sqrt{\frac{T}{T_{c,ij}}} \right) \right]^2,$$
$$b_i = 0.0778 \frac{\mathcal{R} T_{c,i}}{p_{c,i}}, \tag{18}$$

including the pseudo-critical values for non-diagonal elements

$$Z_{c,ij} = 0.5(Z_{c,i} + Z_{c,j}),$$
$$v_{c,ij} = \frac{1}{8} [v_{c,i}^{1/3} + v_{c,j}^{1/3}]^3,$$
$$\omega_{ij} = 0.5(\omega_i + \omega_j), \tag{19}$$
$$T_{c,ij} = \sqrt{T_{c,i} T_{c,j}}(1 - k_{ij}),$$
$$p_{c,ij} = Z_{c,ij}(\mathcal{R} T_{c,ij}/v_{c,ij}).$$

Here, k_{ij} denotes the binary interaction parameter for the pseudo-critical mixing rules, which has to be fitted with experimental data. It has to be noted that all mixing and combining rules are essentially empirical; thus, only a comparison with experimental data gives information about the correctness of the applied methods.[1] Based on the modeling above, the temperature is deduced from the enthalpy and pressure using the method by Dekker (see Refs. 43 and 44). The calculated temperature is based on the mixture fluid, which is also referred to as dense gas approach. In this paper, the obtained temperature is referred to as frozen temperature T_f. This temperature is only a product of the mixture fluid properties and does not include any phase change phenomena.

A mixture of two components results in a critical locus depending on the mixture fraction, as mentioned in Sec. II. As a consequence, subcritical conditions may be present despite supercritical conditions for each individual component, potentially leading to phase-separation. At first, we are evaluating in each cell, if the mixture is at a single-phase or a multi-phase state performing a stability analysis. A mixture is considered stable if the total Gibbs energy is at its global minimum (see Michelsen and Mollerup[45]). The stability analysis is performed by applying the tangent plane distance (TPD) method by

Michelsen and Mollerup.[45] For a mixture with $N \leq 2$ components at a given temperature and pressure, we employ a trial phase composition $\mathbf{w} = [w_1, \ldots, w_N]$ and fugacity coefficient ϕ_i for component i of a composition $\mathbf{z}$. The TPD is defined as follows:

$$TPD(\mathbf{w}) = \sum_{i}^{N_k} w_i \{ \ln w_i + \ln \varphi_i(\mathbf{w}) - \ln z_i - \ln \varphi_i(\mathbf{z}) \}. \tag{20}$$

If $TPD \leq 0$, the mixture is stable and the cubic EOS is solved without a flash calculation. Otherwise, the mixture is in a multi-phase state, thus within the two-phase region. Then, the vapor–liquid phase equilibrium (VLE) is calculated solving the isenthalpic-isobaric-iso-composition flash problem (*hpn*-flash).[18] The resulting temperature is referred to as adiabatic mixing temperature T_{ad}.

IV. SETUP

In this study, the injector types presented in Sec. II are reduced to a two-dimensional planar shear layer (no z-direction) in order to focus on the influence of non-linear thermodynamic effects and phase separation due to multicomponent mixing on a transcritical mixing layer. The geometry is presented in Fig. 4. In the inner $7.5H \times 7.5H$ region, the flow is resolved down to the smallest scales (see Sec. V), whereas for the rest of the $50H \times 50H$ domain, a smooth stretching is applied to prevent an influence of the boundary condition. Only the inner cyan colored region is used for the analysis of the results. Propane is entering the domain at the top and nitrogen at the bottom. Both fluids have a constant velocity in the shape of a block profile, since we put the focus on the thermodynamics and mixing. No fluctuations are superimposed. The two fluids are divided by a splitter plate of height H, which is characteristic for rocket propulsion engines.[46] On the right, top, and bottom, we defined a Neumann boundary condition setting the gradient to zero. The surface of the splitter plate is modeled as a no-slip wall.

We are analyzing three operating points, where we change the temperature or the pressure of each fluid. In order to compare all three
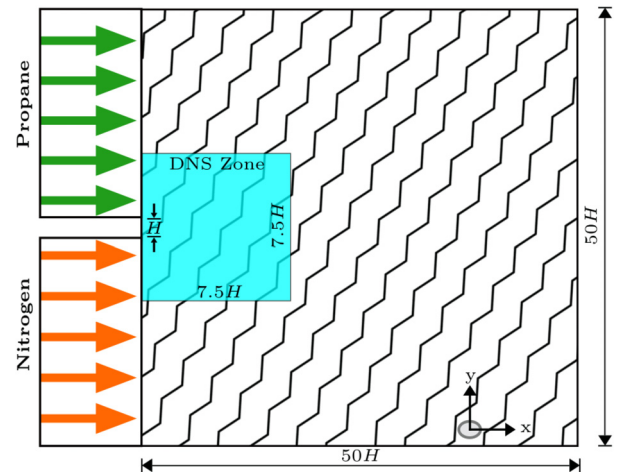

FIG. 4. Sketch of the used two-dimensional domain. Propane is entering at the top and nitrogen at the bottom with a constant velocity. The gap between the two jets is H, which refers to the splitter plate height. The hatched area is the simulation domain and the cyan region marks an equidistant cell distribution with DNS resolution, which is used for the evaluation.

27 June 2024 13:51:33

operating points in a fair manner with each other, we adjusted the velocities of both fluids obtaining a Reynolds number of $Re \approx 1 \times 10^4$ for propane and $Re \approx 2 \times 10^4$ for nitrogen. The Reynolds number Re is evaluated with

$$Re = u_{in} * H / \nu_{in}, \tag{21}$$

where u_{in} denotes the velocity and ν_{in} is the kinematic viscosity at the inlet. The splitter plate height is used as characteristic length. Figure 5 shows phase diagrams based on the mixture fraction and temperature at constant pressure. The two-phase region is enclosed by the bubble- (blue) and dew point (red) lines. By means of the adiabatic mixing temperature and depending on the overall mole fraction z, a liquid and vapor phase coexists in equilibrium.

For the first operating point (two-phase → 2P), the temperature and pressure of propane and nitrogen are set in such a way that the mixture enters the two-phase region shown in Fig. 5(a). As the nitrogen mass fraction increases, T_{ad} crosses the bubble-point line at $z_{N2} \approx 0.1$; hence, entering the two-phase region, where vapor and liquid are in co-existence. As the amount of nitrogen in the mixture rises, the vapor fraction increases until the dew point line, where the mixture consists of 100% vapor and the mixture emerges from the two-phase region. Thus, this operating point is at a two-phase state for $0.1 < z_{N2} < 0.9$ and at a single-phase state for $z_{N2} < 0.1$ and $z_{N2} > 0.9$, respectively.

The second operating point (cut two-phase → C2P) slightly cuts the two-phase region at the dew point line, resulting in a thin two-phase region within the mixing layer, shown in Fig. 5(b).

The last operating point (no two-phase → N2P), the temperature of propane is increased, so that no mixture fraction is found within the two-phase region, resulting in a pure single-phase mixture [see Fig. 5(c)]. The parameters of each operating point are summarized in Table II, and the temperature and pressure of each fluid are included at the top of each sub-figure in Fig. 5.

Figure 6 shows a phase diagram based on the mixture fraction and pressure at a constant temperature of 293 K for case 2P. Here, we included experimental data by Marathe and Sandler.[47] A good agreement is observed between the obtained thermodynamic VLE data using the PR EOS and the experimental data for the dew-point line, whereas the bubble-point line deviates with increasing pressure. We used the experimental data in order to optimize the binary interaction parameter k_{ij} and to reduce the modeling error resulting in $k_{ij,opt} \approx 0.064$ using PR EOS for a propane/nitrogen mixture. The optimization process calculates a bubble-point and dew-point line for a sample k_{ij}, hence the difference between the calculated and experimental VLE data values. This process stops as soon as a threshold of $\Delta k_{ij} < 10^{-4}$ between the new and old interaction parameters is reached. This fitting of the interaction parameter results in an adjustment, especially of the bubble point line, which gets closer to the experimental results. Consequently, the two-phase region within the temperature composition extends, especially at the bubble-point line [see Fig. 5(a)]. The fitted interaction parameter was used for all three operating points.

In Fig. 7, the phase envelopes are presented for various mixture fractions in a pressure/temperature diagram. The two-phase area changes for each mixture fraction. Based on the work by van Konynenburg et al.,[48,49] the mixture phase behavior can be categorized into six types. For alkanes/nitrogen mixtures, type I and III are
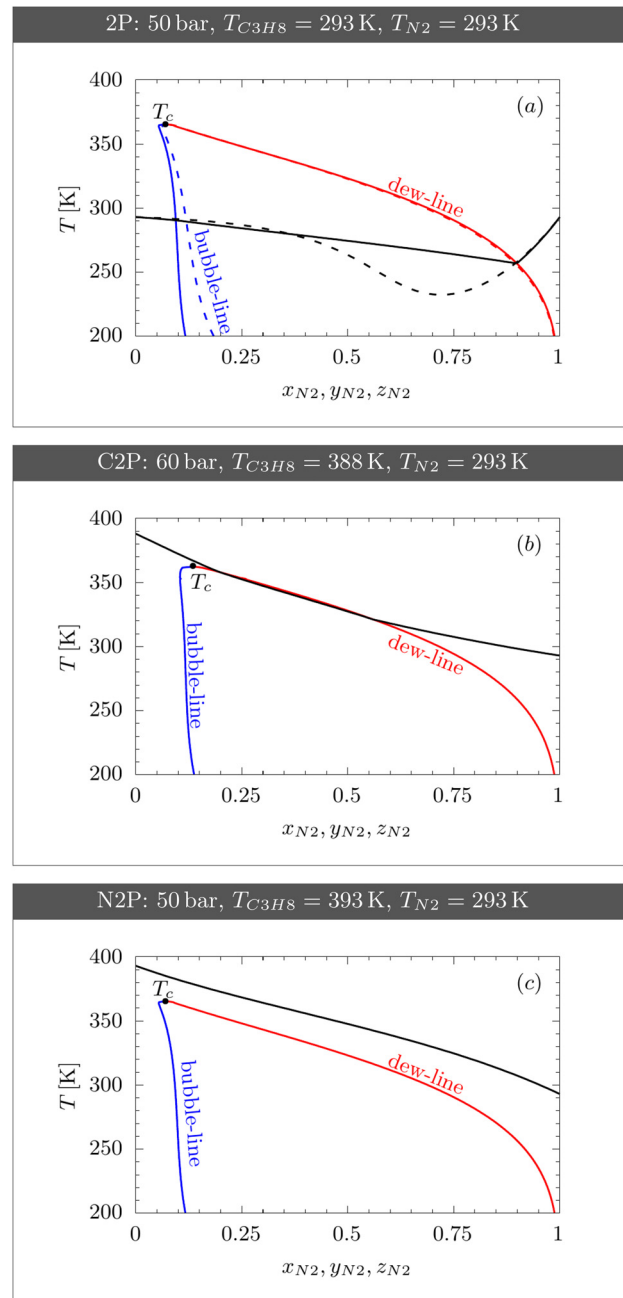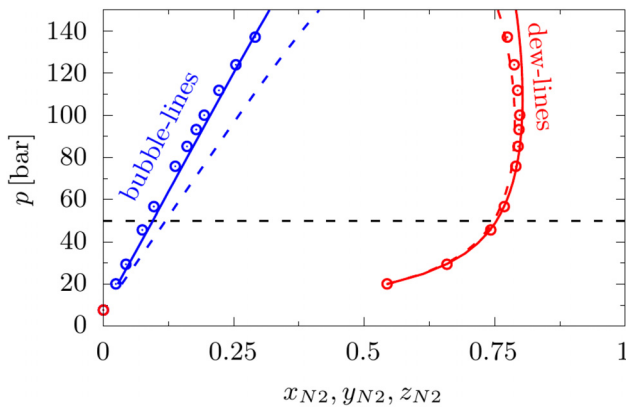

FIG. 5. Phase diagram of binary mixture C_3H_8/N_2 with case 2P in (a), C2P in (b), and case N2P in (c). The adiabatic mixing temperature (black) is presented together with the bubble-point line (blue) and the dew-point line (red). Three operation points are considered with an optimized interaction parameter $k_{ij} = 0.064$. Case 2P (a) includes an interaction parameter of $k_{ij} = 0$ (dashed red/blue) and the frozen temperature T_f (dashed line) where no flash calculation is performed.

essential. A propane/nitrogen mixture belongs to type III, where no continuous critical line is found between the critical points of both single fluids. It can be observed that the dew point line extends to very high pressures.

TABLE II. Operating conditions for all three cases.

	2P	C2P	N2P
p (bar)	50	60	50
T_{C3H8} (K)	293	388	393
T_{N2} (K)	293	293	293
$u_{in,C3H8}$ (m/s)	6.0	2.7	3.1
$u_{in,N2}$ (m/s)	15.0	13.0	15
$\nu_{in,C3H8}$ (m^2/s)	2.44×10^{-7}	1.09×10^{-7}	1.28×10^{-7}
$\nu_{in,N2}$ (m^2/s)	3.11×10^{-7}	2.63×10^{-7}	3.11×10^{-7}
Re_{C3H8}	9849	9892	9690
Re_{N2}	19 291	19 792	19 291

FIG. 6. Phase diagram of binary mixture C_3H_8/N_2 for case 2P with $T = 293$ K for both fluids. The pressure composition is compared with experimental data at $T = 290$ K ($\odot$). z denotes the overall mole fraction, x denotes the liquid, and y denotes the vapor mole fraction. The binary interaction parameter is optimized using experimental data by Marathe *et al.*[47] Solid red/blue line refers to $k_{ij} = 0.064$, and dashed red/blue line refers to $k_{ij} = 0.0$.

V. GRID RESOLUTION

The grid within the DNS zone has approximately 23×10^6 equidistant cells and extends $7.5H$ in the streamwise and transverse directions, respectively.

Based on Kolmogorov theory and homogeneous turbulence, we approximated the dissipative length scale (see Pope[50] and Unnikrishnan *et al.*[31]). Assuming a fluctuation rate of 25% of the velocity difference between the two fluids $\Delta u = u_{in,N2} - u_{in,C3H8}$, we can define a turbulent Reynolds number

$$Re_t = 0.25 \Delta u H / \nu_{in}. \qquad (22)$$

For case N2P, this results in a turbulent Reynolds number of $Re_{t,C3H8} = 9668.75$ for propane and of $Re_{t,N2} = 3834.4$ for nitrogen. The Kolmogorov length scale η can be calculated using the relation between the large energy carrying and the dissipative scales $l/\eta = Re_t^{3/4}$, where l represents the energy containing length scale normalized with the splitter plate height H. Assuming that the large structures are of the order of the splitter plate height results in
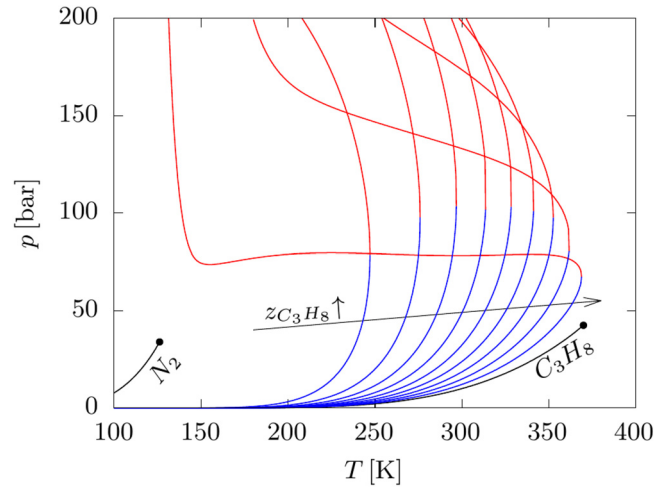
FIG. 7. Phase diagram of binary mixture C_3H_8/N_2. The mixture fraction increases by 10% from left to right. The bubble-point line is indicated in blue, and the dew-point line is indicated in red. The vapor–liquid coexistence line for pure nitrogen and propane is in black.

$\eta \approx 0.001\,03$. According to Pope,[50] an adequate DNS resolution is given by $\Delta x_{Pope} = \pi \eta / 1.5 \approx 0.002\,15$ with $\pi \approx 3.14$.

Since the theoretical deduction for the required resolution is based on ideal gas incompressible, homogeneous turbulent flows,[50] a grid study has been performed. This is in accordance with the study by Sharan and Bellan.[17] In Table III, the size of the DNS zone and its corresponding resolution are listed. Within the DNS region, we prescribe an equidistant cell distribution. In total, five grid levels (LVL0–LVL4) are considered, where we interpolated from the coarse grid to the finer. Our finest grid resolution for LVL4 with $\Delta x/H = 0.001\,56$ is of the order of η and slightly smaller than Δx_{Pope}. We averaged at least over 3 ms after reaching a statistically steady state, which is the smallest averaging time for the finest grid (LVL4) in case N2P. Taking the slowest velocity of 3.1 m/s for N2P results in 3.1 flow through times for the DNS zone of $7.5H$.

In Fig. 8, the mean and root mean square profiles of the velocity in the stream- and spanwise direction and also the density are presented for case N2P. The profiles are normalized with the difference in velocity and density between both fluids, based on the states at the inlet. The values are extracted along the centerline starting at the center of the splitter plate and extending in the streamwise direction x. As it can be seen, LVL2 and LVL3 results are very close to each other,

TABLE III. Grid resolution in the DNS region for the grid study. The grid cells are cubic and equidistant with $\Delta x = \Delta y$.

	Cells in DNS zone	Cell size $\Delta x/H$	Cells over H
LVL0	9×10^4	0.025	40
LVL1	3.6×10^5	0.0125	80
LVL2	1.44×10^6	0.006 25	160
LVL3	5.76×10^6	0.003 13	320
LVL4	23.04×10^6	0.001 56	640
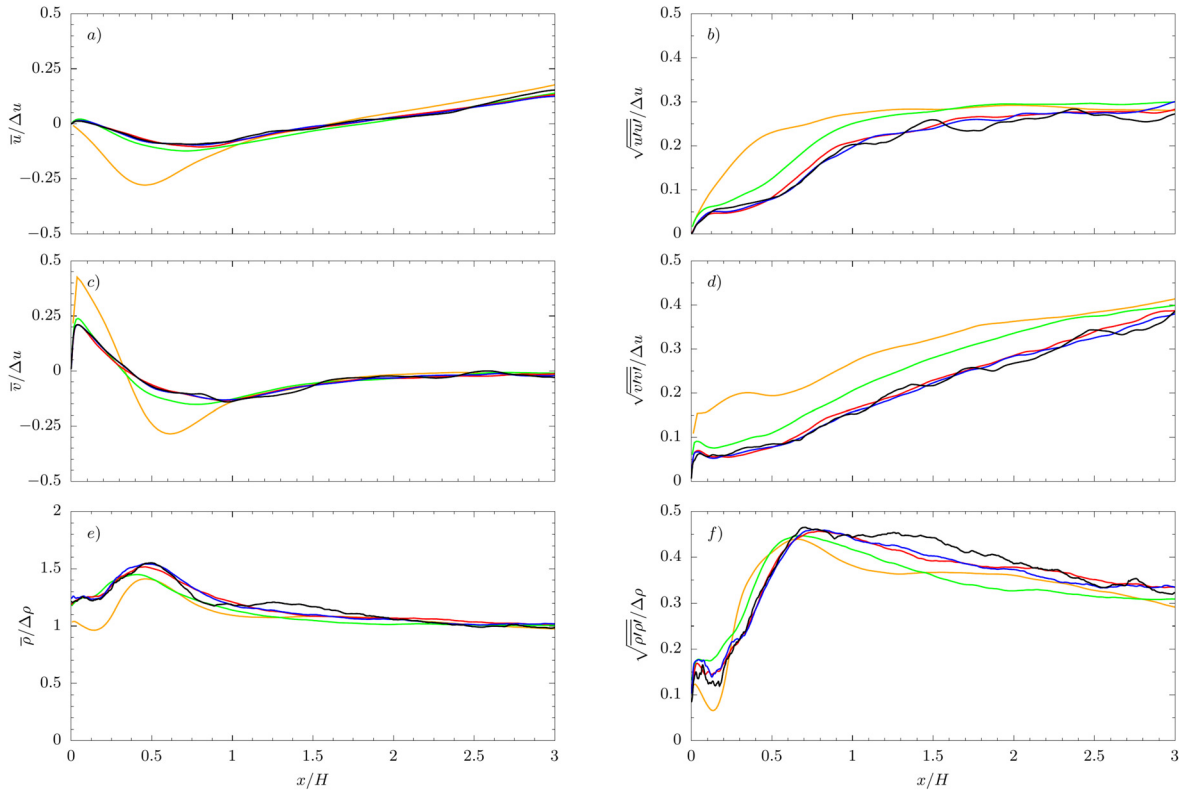
FIG. 8. Mean velocity (a) and (c) and density (e) together with their mean fluctuations (b), (d), and (f) over the centerline in the streamwise direction for case N2P with 50 bar, $T_{C3H8} = 393$ K, $T_{N2} = 293$ K. The distance from the splitter plate is normalized with the splitter plate height H. LVL0 (orange solid line), LVL1 (green solid line), LVL2 (red solid line), LVL3 (blue solid line), and LVL4 (solid line). The profiles are normalized with the difference in velocity and density of both fluids.

indicating a sufficient grid resolution. LVL4 in black has the same trend as the profiles of LVL2 and LVL3 but needs more time to obtain smoother profiles. From this grid analysis, we conclude that the obtained grid resolution of LVL4 with cells of the size of $\Delta x/H = 0.001\,56$ with a uniform distribution within the DNS region is sufficient.

VI. RESULTS

In this section, the results obtained on the finest grid level (LVL4) are presented. General observations are described in Sec. VI A, followed by an analysis of the density ratio between the two streams in Sec. VI B. Furthermore, in Sec. VI C, the vorticity transport is evaluated for all three operating points. Finally, a comparison between equilibrium and frozen hypothesis is performed.

A. General observations

Figure 9 depicts the instantaneous flow field of all three cases. The cases are presented column-wise, with 2P, C2P, and N2P from left to right. For the general comparison, we use various quantities, presented row-wise, with the velocity magnitude (i), the mass fraction of propane (ii), the temperature (iii), the vapor mass fraction (iv), the Prandtl number $Pr = \eta c_p/\lambda$ (v), and the compressibility factor (vi). Propane enters the domain above and nitrogen below the splitter, which is indicated with a green box in Fig. 9. Behind the splitter plate,

a recirculation zone develops. Due to the relatively high Reynolds numbers of both streams, a Kelvin–Helmholtz instability is triggered right away. In the distribution of all three quantities, velocity, propane mass fraction, and temperature, a roll up of the shear layer is observed. The roll up is smoother, less disturbed, or fragmented with increasing temperature of propane, which means from left to right in Fig. 9 or from 2P to N2P.

Before we further analyze this phenomenon and compare it with findings from the literature, additional flow parameters for shear layers are introduced. Various ratios between two streams have been found to be important in order to describe the shear layer behavior. Following Jofre and Urzay,[34] we employ several ratios, which are summarized in Table IV. This includes the ratio of densities

$$\delta_\rho = \rho_{C3H8}/\rho_{N2}, \tag{23}$$
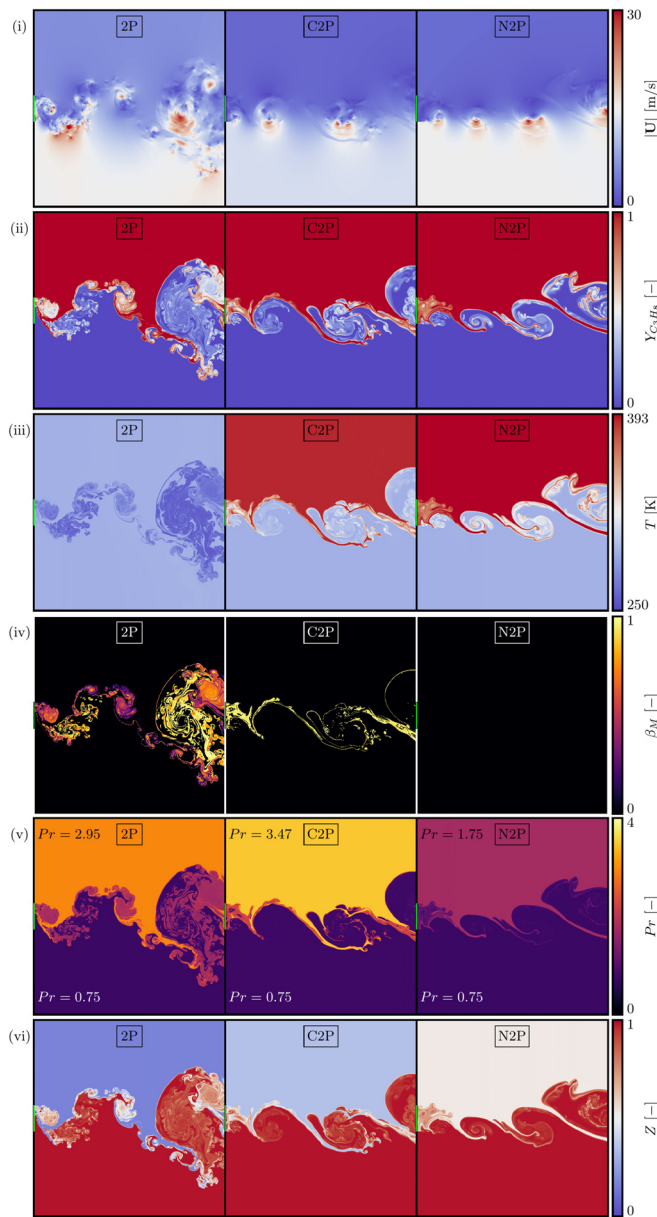
the momentum ratio between the streams

$$\delta_M = (\rho_{C3H8} u_{C3H8}^2)/(\rho_{N2} u_{N2}^2), \tag{24}$$

the velocity ratio

$$\delta_u = u_{C3H8}/u_{N2}, \tag{25}$$

the thermal expansion ratio

$$\delta_\alpha = (T_{C3H8} - T_{N2})/T_{N2}, \tag{26}$$

FIG. 9. Velocity magnitude (i), propane mass fraction Y_{C3H8} (ii), temperature (iii), vapor mass fraction (iv), Prandtl number (v), and compressibility factor (vi) (top to bottom) distributions are shown within the DNS region. The green line indicates the splitter plate.

TABLE IV. Density, momentum, velocity, and thermal expansion ratio for the three cases.

	δ_ρ	δ_M	δ_u	δ_α	δ_μ
2P	9.22	1.45	0.4	0.0	7.23
C2P	3.37	0.15	0.21	0.32	1.40
N2P	2.20	0.09	0.21	0.34	0.91

and the viscosity ratio

$$\delta_\mu = \mu_{C3H8}/\mu_{N2}. \tag{27}$$

It is worth noting that we employ the ratio of the heavier propane, which is at injection either at a liquid (case 2P) or a supercritical liquid-like state (other two cases), to the lighter nitrogen, which is at a supercritical gas-like state at injection for all three cases.

Hoepffner et al.[51] investigated shear layers between a liquid stream, which was static, and a gas stream with a certain velocity. Analyzing the growth of Kelvin–Helmholtz instabilities in shear layers, the vertical speed v and the wave size L are proportional to the density ratio

$$v \propto \sqrt{\rho_g/\rho_l}U, \tag{28}$$

$$L \propto \sqrt{\rho_g/\rho_l}Ut, \tag{29}$$

with velocity U, time t, and the density ratio ρ_g/ρ_l between the gas and the liquid stream. They observed that two vortex sheets are formed along Kaden-like spirals for $\rho_g/\rho_l = 1$. From our performed cases, we observe that case N2P looks similar to the above-described vortex shedding of Hoepffner et al.[51] In the here presented configurations, ρ_g to ρ_l correspond to $1/\delta_\rho$, which is 0.46 for case N2P. This is the highest value and the closest value to 1 among all three cases. On the other hand, for lower $1/\delta_\rho$ values, as for instance case 2P, the wave grows slower and a rather fragmented vortex is created. The snapshots in Fig. 9(i) are in accordance with the observations by Hoepffner et al.[51]

The vortices are connected by longitudinal hairpin-like structures [cf. the propane distribution in Fig. 9(ii)]. Also here the hairpin structures are more perturbed or noisy for 2P than for N2P. Based on the observed behavior, a central role of the density ratio between the two streams can be inferred, as presented by Hoepffner et al.[51] Similar observations have also been made by Ningegowda et al.[28,52] In their 2D study, n-dodecane was mixing faster with nitrogen when the density ratio was increased.

Figures 9(iii) and 9(iv) depict the temperature and the vapor mass fraction distribution. In case 2P, temperature values as low as 254 K are reached in the mixing layer compared to the inlet temperatures of 293 K for propane and nitrogen. This is related to the equilibrium temperature, which decreases within the two-phase dome [see Fig. 5(a)]. At all locations where the temperature is below 293 K, vapor is observed by means of the vapor mass fraction β_M presented in Fig. 9(iv). The full bandwidth of β_M values is found for case 2P where the two-phase dome is entered crossing the bubble-point line and leaving by crossing the dew-point line from the point of view of nitrogen. Since the shear layer for 2P is more fragmented more propane is mixed with nitrogen, a larger area is within the two-phase dome, leading to a higher total amount of vapor in the domain. Case C2P slightly cuts the two-phase dome intersecting the dew-point line, resulting in 100% vapor within the corresponding cells. As a result, a thin layer of vapor can be observed located along the mixing layer. By design, the case N2P is not entering the two-phase dome; thus, the figure shows no vapor content.

The Prandtl number and compressibility factor are shown in rows (v) and (vi) in Fig. 9. As already mentioned in Sec. III, the chosen conditions for nitrogen result in ideal gas condition ($Z = 1$) and a Prandtl number of 0.75. Based on this distribution and conditions, it is
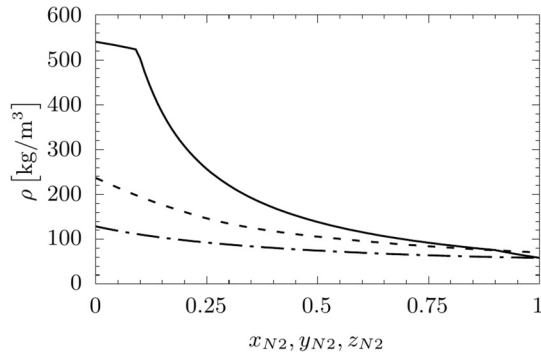
FIG. 10. Density profiles depending on the mixture fraction z_{N2}. Case 2P (——), case C2P (– – – –), and case N2P (– · – · –).

not necessary to solve a real-gas EOS for the whole computational domain. For this reason, tabulated thermodynamic data[25,53,54] could be used to speed up the simulation, since the thermodynamic evaluation including the stability analysis and phase split calculation takes up to 80% of the computational time.

B. Influence of density ratio

As already mentioned above, the density ratio is a crucial parameter for the shear layer dynamics. For this reason, the density depending on the mixture fraction is shown in Fig. 10. For cases C2P and N2P, the density profiles are smooth throughout the mixture, whereas the two-phase dome is clearly visible in case 2P, where the profile has two kinks at around $z_{N2} = 0.1$ and $z_{N2} = 0.95$. The density decreases for pure propane from case 2P to N2P due to the change of operating conditions. Thus, the densities for pure nitrogen and propane at the inlet in case N2P are closer to each other. Hence, the density ratio is reduced, leading to the classical sheet formation as shown in Fig. 9(i) (right).

The partial densities for nitrogen and propane of case 2P are presented in Fig. 11, defined as

$$\rho_{N2} = \rho Y_{N2}, \tag{30}$$

$$\rho_{C3H8} = \rho(1 - Y_{N2}). \tag{31}$$

In both profiles (green line), kinks are visible indicating the two-phase region. Whereas the density for propane is decreasing with increasing nitrogen content, the partial density for nitrogen exhibits a maximum value at the dew-point, followed by a decrease for $0.9 < z_{N2} < 1.0$. Within the two-phase region, the partial density can be further split into their vapor and liquid fraction (see Matheis[55]).

Liquid:

$$\rho_{N2,l} = \rho_l Y_{N2,l}$$
$$\text{with} \quad Y_{N2,l} = x_{N2}M_{N2}/M_l \tag{32}$$
$$\text{and} \quad M_l = x_{N2}M_{N2} + x_{C3H8}M_{C3H8}.$$

Vapor:

$$\rho_{N2,v} = \rho_v Y_{N2,v}$$
$$\text{with} \quad Y_{N2,v} = y_{N2}M_{N2}/M_v \tag{33}$$
$$\text{and} \quad M_v = y_{N2}M_{N2} + y_{C3H8}M_{C3H8}.$$
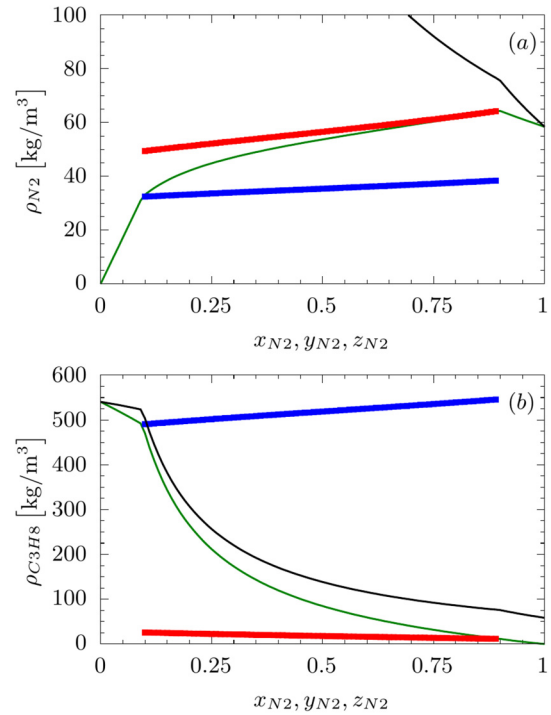
FIG. 11. The partial densities for case 2P are included in (a) for nitrogen and in (b) for propane. Red lines represent the vapor, and the blue lines represent the liquid density. Solid line refers to the overall equilibrium density and the green line to the equilibrium density of nitrogen (a) and propane (b), respectively.

$Y_{N2,l}$ and $Y_{N2,v}$ denote the mass fraction of nitrogen in the liquid and vapor phase, and M_v and M_l are the molar masses of liquid and vapor phases, respectively. The same holds for the propane contribution. The partial density emerging from the phase-separation based on Eqs. (32) and (33) is shown in Fig. 11 in the range of around $0.1 < z_{N2} < 0.9$. Especially propane exhibits a big difference between the liquid and vapor density with a ratio range of $19 < |\Delta\rho_{C3H8,\text{VLE}}| < 47$ compared to nitrogen of $1.5 < |\Delta\rho_{N2,\text{VLE}}| < 1.7$, with $|\Delta\rho_{\text{VLE}}| = |\rho_{liquid} - \rho_{vapour}|$.

The liquid fraction and vapor fraction distributions of propane are presented in Fig. 12. Histograms are added in Fig. 12 to visualize the phase splitting, which is based on all cells with $\beta_M > 0$. The amount of liquid propane at each location with VLE is nearly the same for cases 2P and C2P, despite the varying operating conditions [cf. histograms in Fig. 12(i)]. Thus, the fraction of liquid nitrogen, $x_{N2} \approx 0.1$, is also the same for both cases since $x_{C3H8} + x_{N2} = 1$. On the other hand, the vapor composition differs from 2P to C2P. In case 2P, propane provides 10%–30% of the total vapor content; thus, most of the vapor is nitrogen, since $y_{C3H8} + y_{N2} = 1$. For case C2P, the vapor content is more equally distributed between both fluids compared to 2P [see histograms in Fig. 12(ii)]. Slightly more propane vapor can be observed due to the increase in the histogram between $0.6 < y_{C3H8} < 0.8$.

The magnitude of the density gradient for all three cases in depicted in Fig. 13. The gradient is only large in the contact area between propane and nitrogen. In this contact area, the density
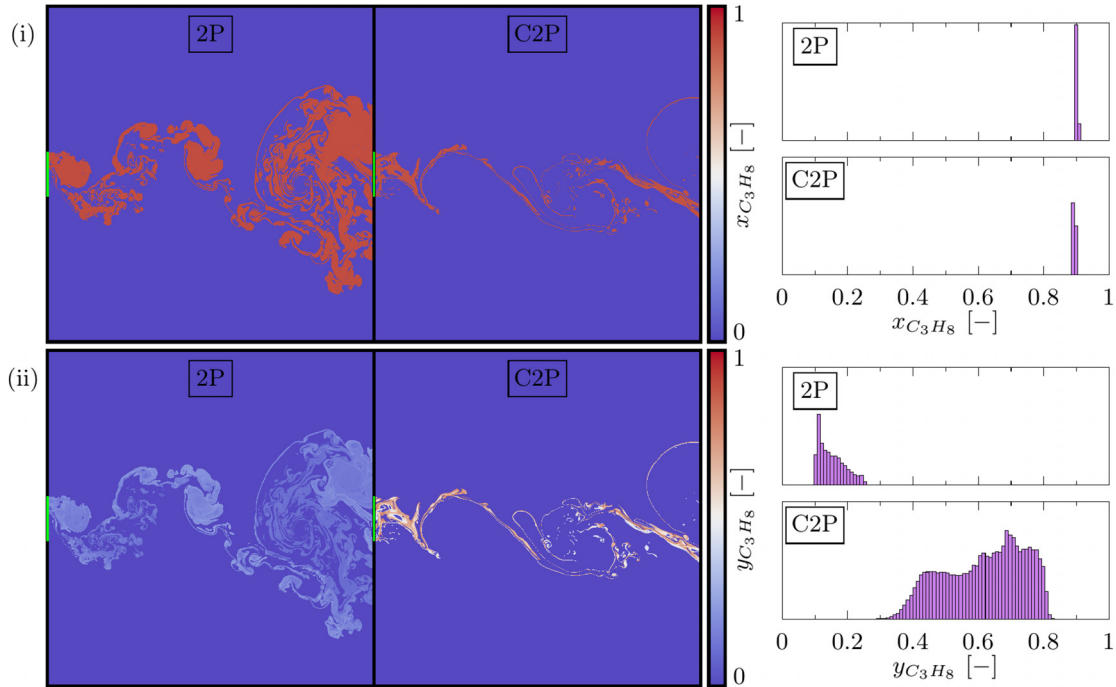
FIG. 12. Liquid fraction (i) and vapor fraction (ii) distribution of propane are shown within the DNS region. The green line indicates the splitter plate. Histograms of the observed values are presented on the right. All cells with $\beta_M > 0$ are considered.
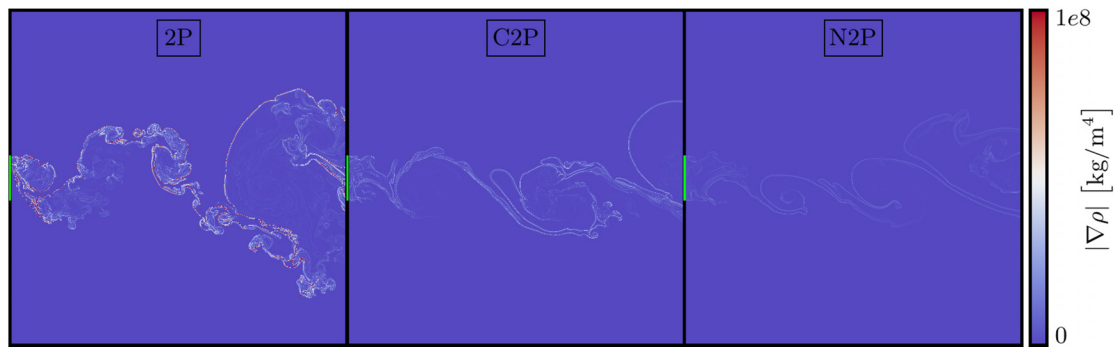
FIG. 13. Magnitude of the density gradient for all three cases within the DNS region. The green line indicates the splitter plate.

gradient $|\nabla\rho|$ sharply rises from 0 to 1.0×10^8 in 2P. This sharp contact area where the propane mass fraction goes from 0 to 1 is resolved with approximately 15 cells in 2P. For the other cases, this interface area is more diffuse and resolved with approximately 36 cells. This in agreement with the intended thermodynamic states, where a sharp interface is obtained in the two-phase region (2P) and a diffuse interface is present for the supercritical case N2P. Similar observations are also made by Ningegowda et al.,[28,52] where the interface is more diffuse for higher inlet temperatures, thus a pure supercritical mixture. Furthermore, the gradient is one order magnitude higher in case 2P with $|\nabla\rho|_{max} = 1.0 \times 10^8$ compared to case N2P with $|\nabla\rho|_{max} = 1.7 \times 10^7$.

C. Analysis of vorticity transport

In the following, we are investigating the distribution of the vorticity vector

$$\omega_i = \nabla \times u_i, \qquad (34)$$

which is inspired by the analysis of a 3D transcritical jet by Koukouvinis et al.[25] In 2D, the vorticity vector has only one non-vanishing component in the z-direction, which is presented in Fig. 14(i). The fragmentation of velocity in the contact area observed for case 2P before is supported by a lot of small vortices, visible by means of ω_z. Compared to case N2P, where only big vortex cores are

27 June 2024 13:51:33
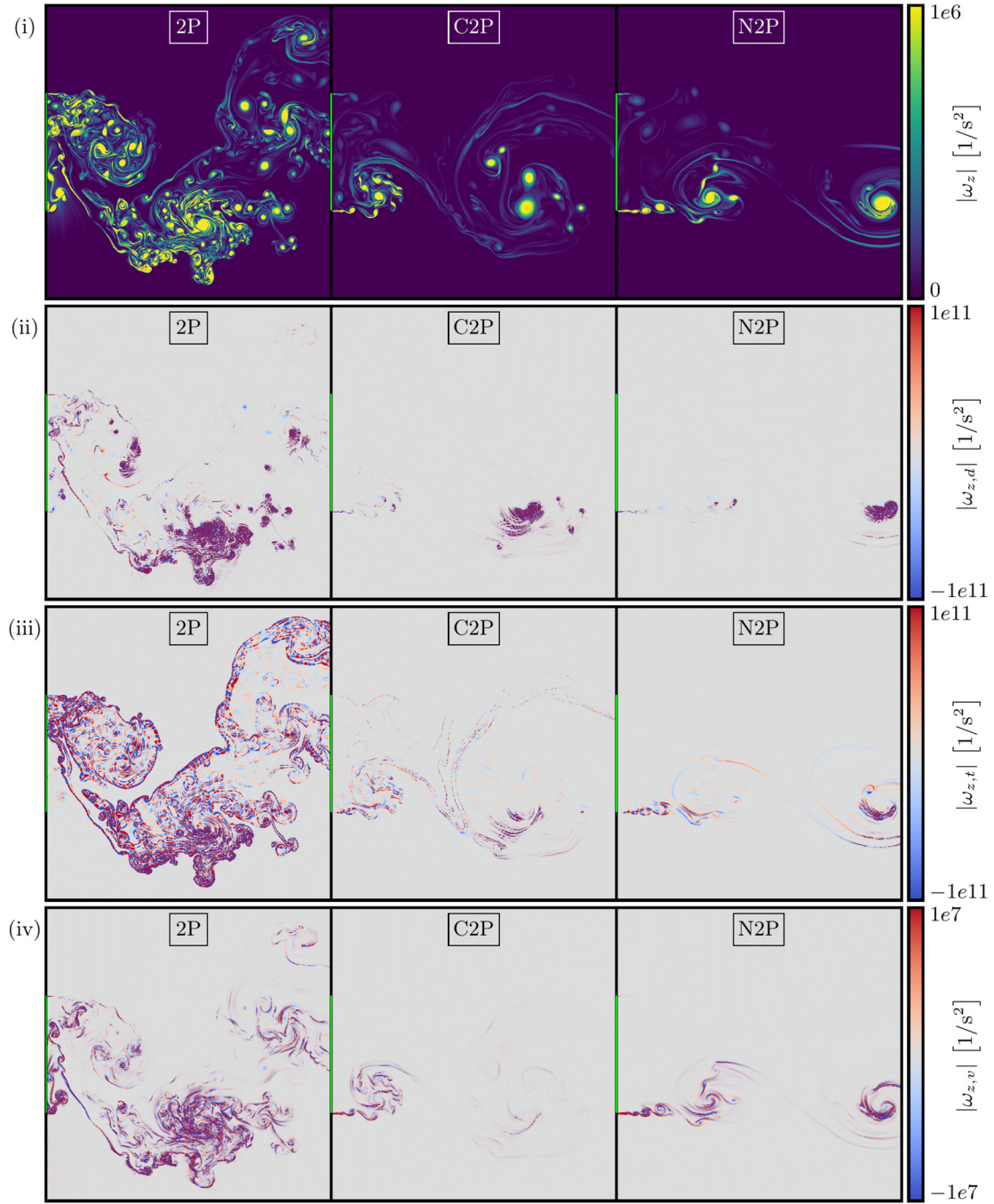
FIG. 14. Vorticity ω_z (i), dilatation of vorticity $\omega_{z,d}$ (ii), baroclinic torque $\omega_{z,t}$ (iii), and diffusion due to viscous effects $\omega_{z,v}$ (iv) (top to bottom). The last three are taken from the vorticity evolution [Eq. (35)]. The shown area is $1.25H$ above and below the centerline ($-1.25H < y < 1.25H$) and $2.5H$ in the streamwise direction taken downstream from the splitter plate ($0 < x < 2.5H$). The green line indicates the splitter plate.

present, a range of vortices with different sizes and intensities are present for case 2P. Smaller sized vortices are especially present in regions where vapor is observed.

The evolution of vorticity is given by the following equation:

$$\frac{\partial \omega}{\partial t} = (\omega \cdot \nabla)u + \underbrace{\omega(\nabla \cdot u)}_{\omega_d} + \underbrace{\frac{1}{\rho^2}\nabla \rho \times \nabla p}_{\omega_t} + \underbrace{\nabla \times \left(\frac{\nabla \cdot \tau}{\rho}\right)}_{\omega_v}, \quad (35)$$

where the first term is the vortex stretching describing the stretching or tilting of vorticity due to the flow velocity gradients. This term is zero in 2 D cases. The second term is the vorticity dilatation ω_d, which describes the stretching of vorticity due to flow compressibility. The third term is the baroclinic torque ω_t, which accounts for the changes in the vorticity due to the intersection of density and pressure surfaces. This term is related to the Rayleigh–Taylor instability. The last term is the diffusion of vorticity ω_v due to viscous effects.

The terms of the aforementioned vorticity evolution equation are presented in Fig. 14. It has to be mentioned that the shown area is reduced from $7.5H \times 7.5H$ to $2.5H \times 2.5H$ for a more detailed view. The shear layer is mainly dominated by vorticity dilatation (ii) and baroclinic torque (iii). Both are linked to the velocity and density ratios presented in Table IV. Vorticity dilatation is only based on velocity gradients; hence, the prescribed velocity ratio δ_u is the decisive parameter for this term leading to Kelvin–Helmholtz instabilities. On the other hand, the baroclinic torque is driven by the density gradient $\nabla\rho$, which is dictated by the imposed density ratio δ_ρ. Consequently, the strength of the baroclinic torque follows the density gradient, as shown in Fig. 13. The intensity and covered area are larger for case 2P compared to C2P and N2P. Vorticity dilatation is dominating, especially in areas where large vortices are located. Both terms ω_d and ω_t are approximately of the same order. Vorticity diffusion (iv) is several orders of magnitude smaller, leading to the conclusion that this contribution can be neglected. These observations are in accordance with the study of a 3D transcritical jet by Koukouvinis et al.[25]

One has to be aware that performing simulations based on a fully conservative formulation in a density based solver may suffer from spurious pressure oscillations,[7–9,13,23] as mentioned in Sec. I. As a consequence, local pressure gradients arise, which alter the baroclinic torque. Thus, the increase in the baroclinic torque enhances the mixing locally, which can distort the results. Since we use a pressure based solver framework in our study, spurious pressure oscillations are omitted.

### D. Comparison of equilibrium and frozen hypothesis

In this section, we compare the result of case 2P with the same case conditions, but the phase split calculation is turned off (2PNF = two-phase no flash). This comparison aims to emphasize the need for a phase-split calculation for the correct prediction of the flow dynamics. As a consequence, the obtained temperature is referred to as *frozen temperature*, which was already shown in the temperature composition diagram of case 2P in Fig. 5. Figures 15(a) and 15(b) show the adiabatic and frozen mixing temperature at a constant pressure of 50 bar and the corresponding data from the DNS simulations by means of black points. The largest deviation between the adiabatic mixing temperature and the frozen temperature is for mixtures between $0.4 < z_{N2} < 0.9$. For these mixtures, the frozen temperature reaches a minimum temperature of 232 K, which is lower compared to the minimal adiabatic mixing temperature of 257 K. Furthermore, the mixture density without flash calculation is higher than the equilibrium mixture density, shown in Fig. 15(c). The spreading of the DNS data points in case 2PNF stems from higher pressure fluctuations compared to 2P. The absolute difference between both densities $|\rho_{ad} - \rho_f|$ is presented in Fig. 15(d). It reaches nearly 250 $kg\,m^{-3}$ at around $z_{N2} = 0.325$. As a consequence, the local density in case 2PNF is
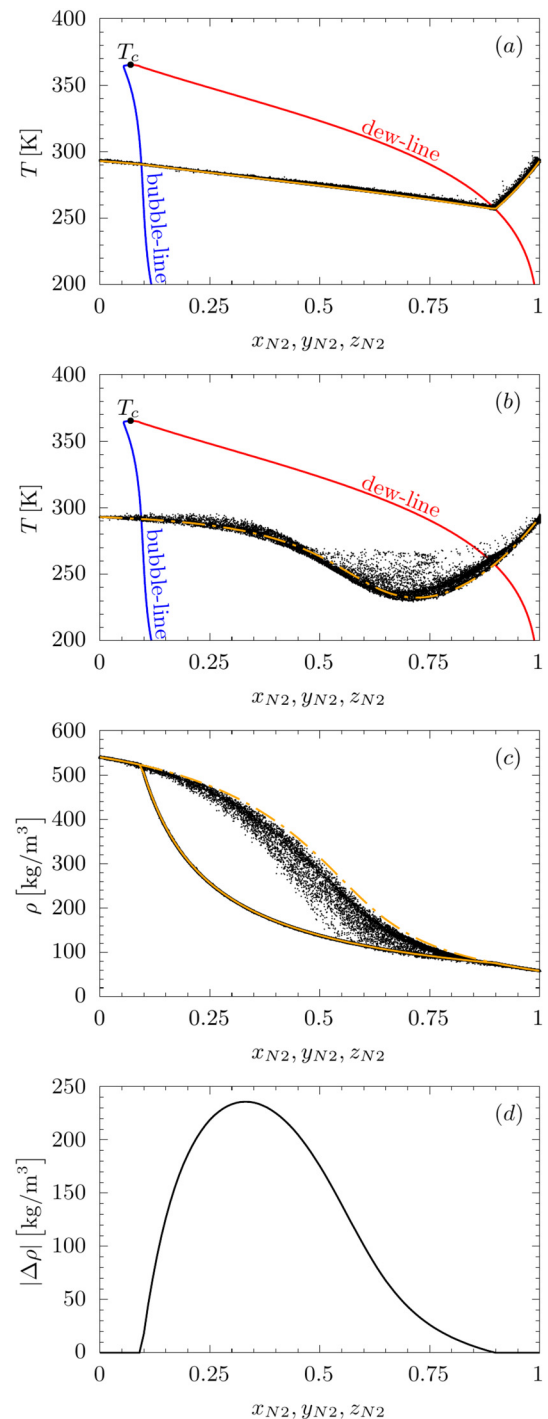

FIG. 15. Temperature composition diagrams in (a) and (b). The orange lines represent the equilibrium temperature (2P = flash calculation) in (a) and the frozen temperature (2PNF = no flash calculation) in (b). The bubble-point line is represented in blue, and the dew-point line is represented in red color. The equilibrium density (solid line) and the frozen density (dashed line) are shown in (c). Black dots are data points from the DNS simulations. The density difference between the frozen and equilibrium density is presented in (d).

leading to a higher density gradient, thus, following the previous observations, to a stronger mixing.

In Fig. 16, snapshots of the absolute velocity (i), propane mass fraction (ii), temperature (iii), and vorticity (iv) of case 2P and 2PNF are presented. The contact area between propane and nitrogen is more wrinkled in case 2PNF compared to case 2P, which supports the conclusion made above. This is observed in the distribution of all four quantities, but especially the vorticity distribution illustrates the difference between both simulations [see Fig. 16(iv)]. Also the lower temperature (iii), which results from the frozen temperature calculation, is clearly visibly in the mixing zone between propane and nitrogen [see
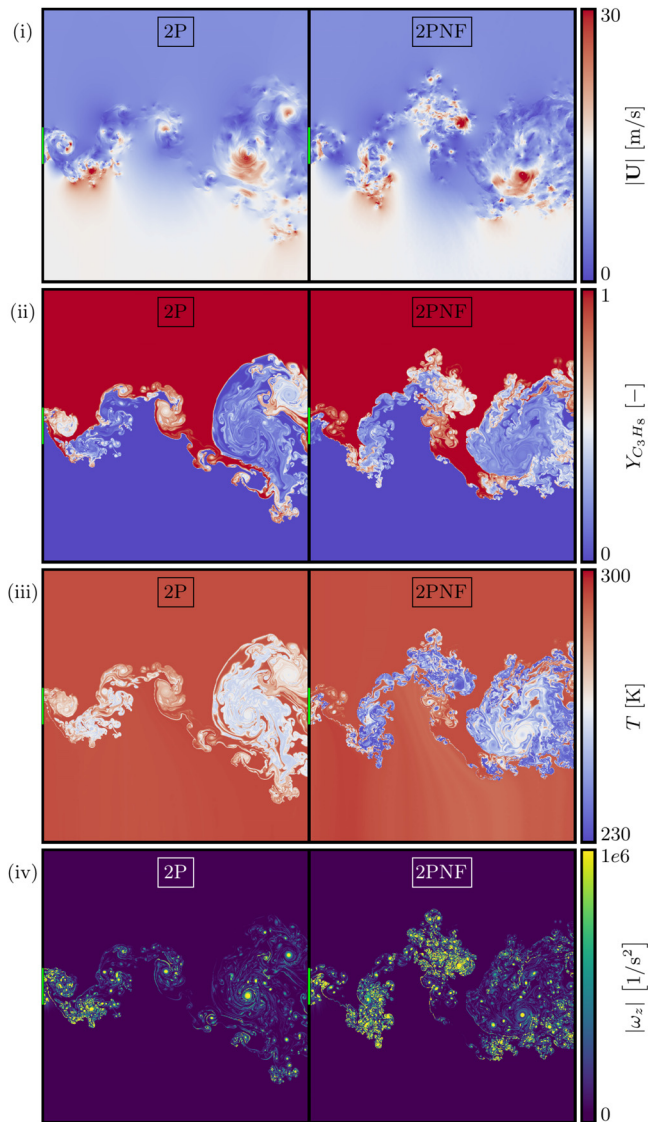
FIG. 16. Velocity magnitude (i), propane mass fraction Y_{C3H8} (ii), temperature (iii), and vorticity distribution (iv) within the DNS region (top to bottom). The green line indicates the splitter plate. The left column refers to case 2P with flash calculation, and the right column refers to case 2PNF without flash calculation.
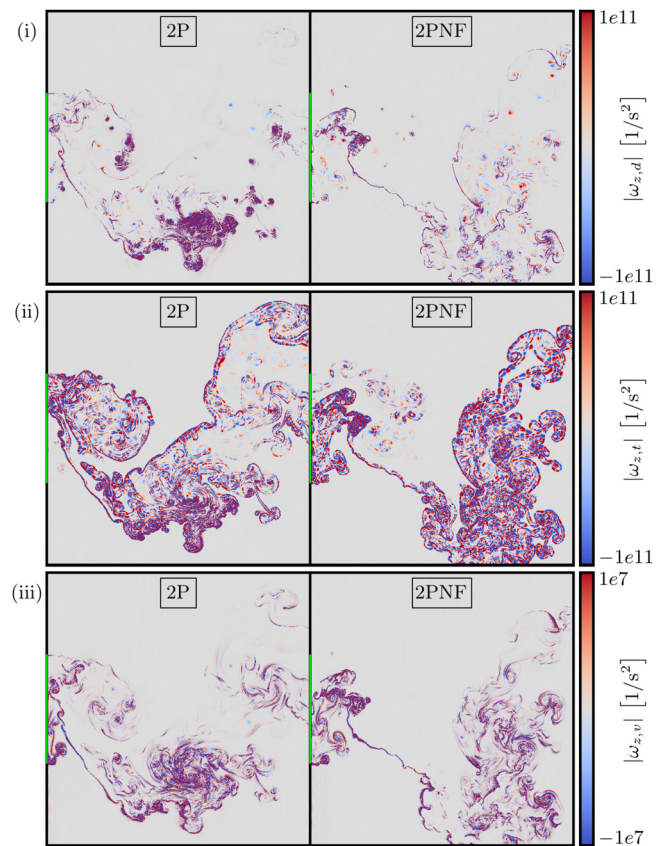
FIG. 17. Terms of the vorticity equation: vorticity dilation (i), baroclinic torque (ii), and viscous diffusion (iii). The green line indicates the splitter plate. The left column refers to case 2P with flash calculation, and the right column refers to case 2PNF without flash calculation. The shown area is $1.25H$ above and below the centerline ($-1.25H < y < 1.25H$) and $2.5H$ in the streamwise direction taken downstream from the splitter plate ($0 < x < 2.5H$).

Fig. 16(iii)]. In Fig. 17, all three terms of the vorticity transport equation are compared between cases 2P and 2PNF. Omitting the phase splitting calculation reduces the dilatation term (i) and the baroclinic torque (ii) covers more area due to the difference in density. Our results are showing the opposite behavior compared to the study by Tudisco and Menon.[14] In their investigation, the shear layer is more distorted when applying VLE. This can be attributed to their modeling of the transport properties, the species diffusion, and the moderate resolution in their simulation. All in all from this comparison, we can conclude that omitting the flash calculation leads to a different density and density gradient; thus, this may enhance or attenuate mixing. In both ways, excluding the VLE may be inaccurate and lead to wrong conclusions.

VII. CONCLUSION

DNS simulations of a 2D planar shear layer, which refers to a coaxial injector, have been used to analyze the influence of multicomponent mixing and VLE on the shear layer dynamics. For this purpose, propane and nitrogen separated by a thin splitter plate have been

mixed. We have conducted the DNS study for three different operating points, which are defined by the fluids' temperature and pressure values, respectively. The first case included VLE (2P), the second contained two-phase phenomena only for a few mixture fractions, and the third avoided VLE (N2P). Using the obtained flow results, we performed thorough analyses of the flow field, considering the velocity, temperature, density, and vorticity distribution. Although the presented 2D DNS study is not able to fully represent the dynamics of turbulence, it is useful to evaluate the influence of different thermodynamic states on a transcritical shear flow.

In each case, a recirculation zone has developed behind the splitter plate. The Kelvin–Helmholtz instability leads directly to a roll up of the shear layer for all three cases. The vortices have been more fragmented, and the more mixture fluid was in a two-phase state, which can be related to the higher density gradient between both fluids. Thus, the density gradient is a key parameter defining the behavior of the shear layer dynamics, independent of the VLE contribution. This is in accordance with single phase shear layers from the literature.

Additionally, our DNS investigation allowed for detailed insight into the composition of the phases. We found that the phase composition differs depending on the crossed two-phase region. The obtained data might serve as comparison data for future experimental studies. The analysis of the vorticity transport equation revealed that the vorticity dilation and the baroclinic torque are prevalent, whereas viscous effects are several orders of magnitude smaller. Similar proportions have been observed for a transcritical 3 D jet in the literature.

Finally, we have used the operating conditions of case 2P and turned off the phase splitting calculations (2PNF) in order to analyze the importance of VLE. The comparison between 2P and 2PNF has revealed a large difference in density up to $250\,\mathrm{kg\,m^{-3}}$. This difference in density has affected the baroclinic torque, which has led to more fragmentation with an increased amount of smaller vortices for case 2PNF.

In summary, the velocity and density ratio are responsible for the vorticity dilation and the baroclinic torque. Thus, these ratios are controlling the dynamics of the shear layer. Consequently, VLE has to be considered in order to capture the correct density, which has a leading role. This DNS study provided detailed insight of transcritical shear layer flows, which have a higher resolution than any experiment and can be used for the testing and development of low-cost CFD models.

ACKNOWLEDGMENTS

AUTHOR DECLARATIONS
Conflict of Interest

The authors have no conflicts to disclose.

Author Contributions

Alexander Doehring: Conceptualization (equal); Formal analysis (equal); Investigation (equal); Methodology (equal); Software (equal); Validation (equal); Visualization (equal); Writing – original draft (equal); Writing – review & editing (equal). **Theresa Trummler:** Conceptualization (equal); Methodology (equal); Project administration (equal); Resources (equal); Software (equal); Writing – review & editing (equal). **Michael Pfitzner:** Funding acquisition (equal); Writing – review & editing (equal). **Markus Klein:** Project administration (equal); Supervision (equal); Writing – review & editing (equal).

DATA AVAILABILITY

The data that support the findings of this study are available from the corresponding author upon reasonable request.

REFERENCES

[1]B. E. Poling, J. M. Prausnitz, and J. P. O'connell, *The Properties of Gases and Liquids* (McGraw-Hill, New York, 2001), Vol. 5.
[2]W. Mayer and H. Tamura, "Propellant injection in a liquid oxygen/gaseous hydrogen rocket engine," J. Propul. Power **12**, 1137–1147 (1996).
[3]M. Oschwald, J. J. Smith, R. Branam, J. Hussong, A. Schik, B. Chehroudi, and D. Talley, "Injection of fluids into supercritical environments," Combust. Sci. Technol. **178**, 49–100 (2006).
[4]B. Chehroudi, "Recent experimental efforts on high-pressure supercritical injection for liquid rockets and their implications," Int. J. Aerosp. Eng. **2012**, 121802.
[5]S. Baab, C. Steinhausen, G. Lamanna, B. Weigand, and F. J. Förster, "A quantitative speed of sound database for multi-component jet mixing at high pressure," Fuel **233**, 918–925 (2018).
[6]N. A. Okong'o and J. Bellan, "Direct numerical simulation of a transitional supercritical binary mixing layer: Heptane and nitrogen," J. Fluid Mech. **464**, 1–34 (2002).
[7]J.-P. Hickey, P. C. Ma, M. Ihme, and S. S. Thakur, "Large eddy simulation of shear coaxial rocket injector: Real fluid effects," in *49th AIAA/ASME/SAE/ASEE Joint Propulsion Conference* (AIAA, 2013), p. 4071.
[8]H. Terashima, S. Kawai, and N. Yamanishi, "High-resolution numerical method for supercritical flows with large density variations," AIAA J. **49**, 2658–2672 (2011).
[9]H. Terashima and M. Koshi, "Approach for simulating gas–liquid-like flows under supercritical pressures using a high-order central differencing scheme," J. Comput. Phys. **231**, 6907–6923 (2012).
[10]P. C. Ma, Y. Lv, and M. Ihme, "An entropy-stable hybrid scheme for simulations of transcritical real-fluid flows," J. Comput. Phys. **340**, 330–357 (2017).
[11]G. Lacaze, T. Schmitt, A. Ruiz, and J. C. Oefelein, "Comparison of energy-, pressure- and enthalpy-based approaches for modeling supercritical flows," Comput. Fluids **181**, 35–56 (2019).
[12]J. Matheis and S. Hickel, "Multi-component vapor-liquid equilibrium model for LES of high-pressure fuel injection and application to ECN Spray A," Int. J. Multiphase Flow **99**, 294–311 (2018).
[13]P. C. Ma, H. Wu, D. T. Banuti, and M. Ihme, "On the numerical behavior of diffuse-interface methods for transcritical real-fluids simulations," Int. J. Multiphase Flow **113**, 231–249 (2019).
[14]P. Tudisco and S. Menon, "A vapor–liquid equilibrium induced Lewis number effect in real-gas shear layers: A theoretical study," Phys. Fluids **32**, 112111 (2020).
[15]M. Fathi, S. Hickel, and D. Roekaerts, "Large eddy simulations of reacting and non-reacting transcritical fuel sprays using multiphase thermodynamics," Phys. Fluids **34**, 085131 (2022).

27 June 2024 13:51:33

[16]M. Fathi and S. Hickel, "Rapid multi-component phase-split calculations using volume functions and reduction methods," AIChE J. **67**, e17174 (2021).

[17]N. Sharan and J. Bellan, "Investigation of high-pressure turbulent jets using direct numerical simulation," J. Fluid Mech. **922**, A24 (2021).

[18]C. Traxinger, M. Pfitzner, S. Baab, G. Lamanna, and B. Weigand, "Experimental and numerical investigation of phase separation due to multicomponent mixing at high-pressure conditions," Phys. Rev. Fluids **4**, 074303 (2019).

[19]A. Begemann, T. Trummler, A. Doehring, M. Pfitzner, and M. Klein, "Assessment of the thermodynamic and numerical modeling of les of multi-component jet mixing at high pressure," Energies **16**, 2113 (2023).

[20]J. Gross and G. Sadowski, "Perturbed-chain SAFT: An equation of state based on a perturbation theory for chain molecules," Ind. Eng. Chem. Res. **40**, 1244–1260 (2001).

[21]J. Gross and G. Sadowski, "Application of the perturbed-chain SAFT equation of state to associating systems," Ind. Eng. Chem. Res. **41**, 5510–5515 (2002).

[22]R. Stierle, E. Sauer, J. Eller, M. Theiss, P. Rehner, P. Ackermann, and J. Gross, "Guide to efficient solution of PC-SAFT classical density functional theory in various coordinate systems using fast Fourier and similar transforms," Fluid Phase Equilibria **504**, 112306 (2020).

[23]C. Rodriguez, A. Vidal, P. Koukouvinis, M. Gavaises, and M. A. McHugh, "Simulation of transcritical fluid jets using the PC-SAFT EOS," J. Comput. Phys. **374**, 444–468 (2018).

[24]C. Rodriguez, H. B. Rokni, P. Koukouvinis, A. Gupta, and M. Gavaises, "Complex multicomponent real-fluid thermodynamic model for high-pressure diesel fuel injection," Fuel **257**, 115888 (2019).

[25]P. Koukouvinis, A. Vidal-Roncero, C. Rodriguez, M. Gavaises, and L. Pickett, "High pressure/high temperature multiphase simulations of dodecane injection to nitrogen: Application on ECN Spray-A," Fuel **275**, 117871 (2020).

[26]See https://ecn.sandia.gov/for Engine Combustion Network.

[27]T. Schmitt, "Large-eddy simulations of the Mascotte test cases operating at supercritical pressure," Flow. Turbul. Combust. **105**, 159–189 (2020).

[28]B. M. Ningegowda, F. N. Z. Rahantamialisoa, J. Zembi, A. Pandal, H. G. Im, and M. Battistoni, "Large eddy simulations of supercritical and transcritical jet flows using real fluid thermophysical properties," SAE Technical Paper 2020-01-1153 (2020).

[29]M. Ihme, P. C. Ma, and L. Bravo, "Large eddy simulations of diesel-fuel injection and auto-ignition at transcritical conditions," Int. J. Engine Res. **20**, 58–68 (2019).

[30]P. Tudisco and S. Menon, "Numerical investigations of phase-separation during multi-component mixing at super-critical conditions," Flow. Turbul. Combust. **104**, 693–724 (2020).

[31]U. Unnikrishnan, H. Huo, X. Wang, and V. Yang, "Subgrid scale modeling considerations for large eddy simulation of supercritical turbulent mixing and combustion," Phys. Fluids **33**, 075112 (2021).

[32]R. N. Dahms and J. C. Oefelein, "On the transition between two-phase and single-phase interface dynamics in multicomponent fluids at supercritical pressures," Phys. Fluids **25**, 092103 (2013).

[33]P. Gaillard, V. Giovangigli, and L. Matuszewski, "A diffuse interface lox/hydrogen transcritical flame model," Combust. Theory Modell. **20**, 486–520 (2016).

[34]L. Jofre and J. Urzay, "Transcritical diffuse-interface hydrodynamics of propellants in high-pressure combustors of chemical propulsion systems," Prog. Energy Combust. Sci. **82**, 100877 (2021).

[35]T. Schmitt, Y. Méry, M. Boileau, and S. Candel, "Large-eddy simulation of oxygen/methane flames under transcritical conditions," Proc. Combust. Inst. **33**, 1383–1390 (2011).

[36]H. Müller, C. A. Niedermeier, J. Matheis, M. Pfitzner, and S. Hickel, "Large-eddy simulation of nitrogen injection at trans-and supercritical conditions," Phys. Fluids **28**, 015102 (2016).

[37]D.-Y. Peng and D. B. Robinson, "A new two-constant equation of state," Ind. Eng. Chem. Fund. **15**, 59–64 (1976).

[38]T. H. Chung, M. Ajlan, L. L. Lee, and K. E. Starling, "Generalized multiparameter correlation for nonpolar and polar fluid transport properties," Ind. Eng. Chem. Res. **27**, 671–679 (1988).

[39]A. Burcat and B. Ruscic, "Third millenium ideal gas and condensed phase thermochemical database for combustion (with update from active thermochemical tables)," Technical Rep. ANL-05/20 (2005).

[40]I. H. Bell, J. Wronski, S. Quoilin, and V. Lemort, "Pure and pseudo-pure fluid thermophysical property evaluation and the open-source thermophysical property library CoolProp," Ind. Eng. Chem. Res. **53**, 2498–2508 (2014).

[41]T. Trummler, M. Glatzle, A. Doehring, N. Urban, and M. Klein, "Thermodynamic modeling for numerical simulations based on the generalized cubic equation of state," Phys. Fluids **34**, 116126 (2022).

[42]K. G. Harstad, R. S. Miller, and J. Bellan, "Efficient high-pressure state equations," AIChE J. **43**, 1605–1610 (1997).

[43]W. H. Press, S. A. Teukolsky, W. T. Vetterling, and B. P. Flannery, *Numerical Recipes in C* (Cambridge University Press, Cambridge, 1992).

[44]C. Traxinger, "Real-gas effects and single-phase instabilities during injection, mixing and combustion under high-pressure conditions," Ph.D. thesis (Universität Der Bundeswehr München, 2021).

[45]M. L. Michelsen and J. Mollerup, *Thermodynamic Modelling: Fundamentals and Computational Aspects* (Tie-Line Publications, 2004).

[46]R. Arnold, D. Suslov, and O. J. Haidn, "Circumferential film cooling effectiveness in a lox/h2 subscale combustion chamber," J. Propul. Power **25**, 760–770 (2009).

[47]P. Marathe and S. I. Sandler, "High-pressure vapor-liquid equilibrium of some binary mixtures of cyclopentane, argon, nitrogen, N-butane, and neopentane," J. Chem. Eng. Data **36**, 192–197 (1991).

[48]P. H. van Konynenburg, "Critical lines and phase equilibria in binary mixtures," Ph.D. thesis (University of California, 1968).

[49]P. H. van Konynenburg and R. L. Scott, "Critical lines and phase equilibria in binary van der Waals mixtures," Philos. Trans. R. Soc. London Ser. A, Math. Phys. Sci. **298**, 495–540 (1980).

[50]S. B. Pope, *Turbulent Flows* (Cambridge University Press, 2000).

[51]J. Hoepffner, R. Blumenthal, and S. Zaleski, "Self-similar wave produced by local perturbation of the Kelvin-Helmholtz shear-layer instability," Phys. Rev. Lett. **106**, 104502 (2011).

[52]B. M. Ningegowda, F. N. Z. Rahantamialisoa, P. A. H. Jasak, H. G. Im, and M. Battistoni, "Numerical modeling of transcritical and supercritical fuel injections using a multi-component two-phase flow model," Energies **13**(21), 5676 (2020).

[53]F. Föll, T. Hitz, C. Müller, C.-D. Munz, and M. Dumbser, "On the use of tabulated equations of state for multi-phase simulations in the homogeneous equilibrium limit," Shock Waves **29**, 769–793 (2019).

[54]S. Jafari, H. Gaballa, C. Habchi, J.-C. De Hemptinne, and P. Mougin, "Exploring the interaction between phase separation and turbulent fluid dynamics in multi-species supercritical jets using a tabulated real-fluid model," J. Supercritical Fluids **184**, 105557 (2022).

[55]J. Matheis, "Numerical simulation of fuel injection and turbulent mixing under high-pressure conditions," Ph.D. thesis (Technische Universität München, 2018).

[56]P. Neumann, A. Sharma, L. Viot, T. Trummler, A. Doehring, M. Son, T. Sander, M. Pfitzner, L. Zigan, M. Klein *et al.*, *MaST: Scale-Bridging Exploration of Transcritical Fluid Systems* (Universitat der Bundeswehr Hamburg, 2022).

27 June 2024 13:51:33